Available online at www.sciencedirect.com
ScienceDirect
International Journal of Heat and Fluid Flow 28 (2007) 1484–1491
International Journal of HEAT AND FLUID FLOW
www.elsevier.com/locate/ijhff

Numerical simulation of compressible gas flow and heat transfer in a microchannel surrounded by solid media

Jianhua Zhou, Yuwen Zhang *, J.K. Chen

Department of Mechanical and Aerospace Engineering, University of Missouri-Columbia Columbia, MO 65211, USA

Received 21 September 2006; received in revised form 5 January 2007; accepted 12 March 2007
Available online 17 April 2007

Abstract

In this study, a numerical model is developed to investigate the coupled compressible gas flow and heat transfer in a microchannel surrounded by solid media. To accommodate the varying flow cross-section, the compressible gas flow model is established in a non-orthogonal curvilinear coordinate system. An iterative numerical procedure is employed to solve the coupled heat transfer and gas flow equations. The computer code for the compressible gas flow is first validated against two test problems, and then extended by including the heat conduction in the solid media. The effect of the inlet Mach number on the Nusselt number is examined. It is found that the pressure difference from the pyrolysis front to the heated surface is induced essentially by the gas addition from the channel wall, instead from the pyrolysis front. The necessity of accounting for the gas compressibility is clearly demonstrated when severe heating is applied. The pressure distribution obtained along the channel axial direction is useful for further structural analysis of composite materials.

Keywords: Heat transfer; Compressible flow; Microchannel; Composite material; Pyrolysis

1. Introduction

High-intensity lasers have been widely used in various scientific and engineering areas, such as laser etching and ablation of polyimide (Brannon et al., 1985; Sobehart, 1993), laser ablation of biological tissues (Lane et al., 1986; Lecartentier et al., 1993), thermomechanical failure of composite materials exposed to severe localized heating (Chen et al., 1995), etc. For these applications, scientists and engineers frequently encounter the problem of coupled compressible gas flow and heat transfer in a microchannel surrounded by solid media. For example, during laser processing of polyimide, the intense local heating can result in a strong pyrolysis reaction. The pyrolyzed gas flows outward from the pyrolysis zone toward the polyimide surface at very high velocities (Brannon et al., 1985). Similar situation can be found in the case of laser machining of the composite materials. The outgassing flow effect will cool the surrounding solid media and inhibit the heat transfer into the target. Without considering the gas flow effect, one cannot precisely predict the through-thickness transient temperature distribution, which is a prerequisite for modeling of the subsequent laser ablation.

To correctly describe the gas flow and heat transfer in a microchannel surrounded by solid media caused by rapid heating, four important aspects need to be taken into account. First, the resulting gas should be compressible. For the applications involved high-intensity laser heating, the temperature induced in the irradiated material could be very high, say 2000–3000 °C. As a result, there can be a significant variation in the density of the pyrolysis gas. Therefore, the compressibility effect of the pyrolysis gas should be considered. Second, the gas flows in a microchannel. For example, the space among randomly distributed fibers in an organic composite material usually is from several microns to a millimeter, which is usually referred to as ''microscale''. This kind of problem is usually characterized by a low Reynolds number, which needs special care in the numerical approach. Third, the cross-sectional area of the

* Corresponding author. Tel.: +1 573 884 6936; fax: +1 573 884 5090.
E-mail address: zhangyu@missouri.edu (Y. Zhang).

0142-727X/$ - see front matter © 2007 Elsevier Inc. All rights reserved.
doi:10.1016/j.ijheatfluidflow.2007.03.001

Nomenclature

c_p	heat capacity at constant pressure, J/(kg K)
D	diameter of the gas channel, m
h	surface natural convection coefficient, W/(m^2 K)
h_{sg}	convection heat transfer coefficient at the solid–gas interface, W/(m^2 K)
J	Jacobian determinant
k	thermal conductivity, W/(m K)
L	thickness of the material, m
M	molecular weight, kg/mol
Nu	Nusselt number
p	pressure, N/m^2
Pr	Prandtl number
q''	heating flux, W/m^2
q''_{rad}	radiation heat transfer cooling at the heated surface, W/m^2
t	time, s
T	temperature, K
T_∞	ambient temperature, K
x, r	coordinates in cylindrical coordinate system, m
U, V	contravariant velocity components, m/s
u, v	velocity components in the axial and radial direction, respectively, m/s
$\mathbf{V}$	velocity vector, m/s

Greek symbols

γ	heat capacity ratio
(ξ,η)	non-orthogonal curvilinear coordinates, m
μ	dynamic viscosity, kg/(m s)
ε_{surf}	surface emissivity
ρ	density, kg/m^3
∇	divergence operator

Subscripts

i	initial
in	inlet
g	gas
out	outlet
s	solid

flow channel may change along the longitudinal flowing direction. It is more reasonable to describe the compressible gas flow in a curvilinear coordinate system, not in a rectangular one. Finally, the gas-flowing microchannel is surrounded by the solid material. The overall heat transfer problem is coupled, in which the gas flow in the microchannel is conjugated with the heat conduction in the surrounding solid material.

Based on the aforementioned four physical aspects, the problem needs to be solved by coupling the compressible gas flow and heat transfer in a microchannel surrounded by solid media. However, up to date, little work has been done to understand the fundamental mechanisms in such a coupled heat and mass transfer in a micro flow system. Although some of the previous investigators studied the gas flow in a microchannel, most of the works did not take into account the compressibility effect (e.g., Toh et al., 2002) or not consider the coupled heat transfer effect (e.g., Chen, 2004). Therefore, a quantitative mathematical model including the compressible gas flow effect is needed for accurately predicting the temperature transients of solid target subject to rapid heating.

This paper presents a numerical study on the coupled compressible gas flow and heat transfer in a microchannel surrounded by solid media. To accommodate the varying flow cross-section, the numerical model for the compressible flow is established in a non-orthogonal curvilinear coordinate system. Since the flow and heat transfer are tightly coupled, an iterative numerical procedure must be introduced to determine the heat transfer at the interface. Then, the numerical code is validated against two test problems of subsonic and supersonic flow. Using the present algorithm, numerical simulation is performed for the coupled flow and heat transfer behavior in a microchannel surrounded by a solid medium.

2. Model description

This study deals with the gas flow and heat transfer through a microchannel surrounded by solid media. A generic model is shown in Fig. 1. A finite slab with a

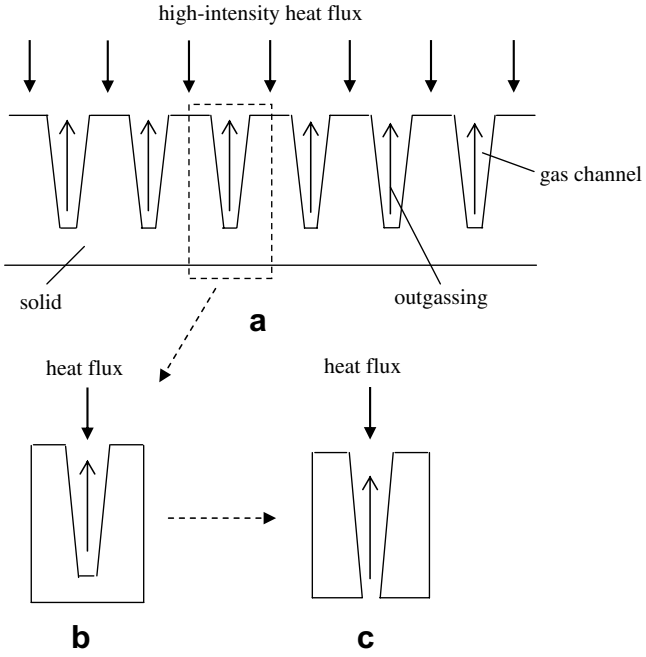

Fig. 1. Physical model.

thickness of L and an initial temperature of T_i is subjected to an intensive heat flux q''. When the temperature in the material is elevated to the pyrolysis onset temperature, the pyrolyzed products are ejected as the gas flows outward from the pyrolysis zone toward the heated surface.

Let us consider the entire material as a great number of the inter-separated gas flow channels surrounded by the un-pyrolyzed solid materials. Each gas flow channel, together with its immediately surrounding material, constitutes an element (shown in the dash-line box of Fig. 1a, as zoomed out in Fig. 1b) The diameter of each element is in the order or microns. Without loss of essential physics, the blind channel shown in Fig. 1b can be further simplified as a through channel, as shown in Fig. 1c.

The axisymmetric feature of the model indicates that a cylindrical coordinate system is the best choice (as shown in Fig. 2). The geometrical parameters and the boundary conditions, which will be further explained later in this paper, are also indicated in Fig. 2. The gas–solid interface shown in Figs. 1 and 2 is cone-shaped although in reality, it is usually irregular. To accommodate the case of irregular gas channel shape, it is required to describe the mathematics in a general curvilinear coordinate system since the heat transfer simulations are performed separately for the gas region and solid region.

For the fluid flow in a microchannel, if the characteristic dimension of the channel is too small, the Knudsen number (which is defined as λ/L_c, where λ is the mean free path of the molecules and L_c is a characteristic length scale) will increase to a very large value. Under this circumstance, some microscopic flow effects (e.g., rarefaction) will become significant and the macroscopic Navier–Stokes equation will break down (Harley et al., 1995; Beskok and Karniadakis, 1999). The gas mean free path λ can be calculated using $\lambda = \mu\sqrt{\pi}/\sqrt{2\rho p}$ (Schaff and Chambre, 1961), where μ is the gas dynamic viscosity, π is the circular constant, ρ is the density and p is the pressure. For the physical properties of gas used in this study, the mean free path λ is on the order of 10^{-11}, which leads to a Knudsen number on the order of 10^{-6} if L_c is set as the diameter of the flow channel. Since such a Knudsen number is much less than 10^{-3}, the gas can be considered as a continuum (Beskok and Karniadakis, 1999). Therefore, the traditional Navier–Stokes equations and no-slip boundary condition can be applied without any modifications.

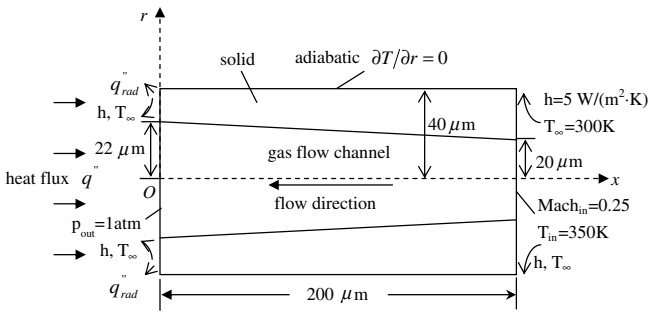

Fig. 2. Cylindrical coordinate system.

The continuity, momentum and energy equations for the 2D axisymmetric laminar and compressible gas flow can be expressed as follows (Kays and Crawford, 1980).

Continuity:

$$\frac{\partial \rho}{\partial t} + \frac{\partial}{\partial x}(\rho u) + \frac{1}{r}\frac{\partial}{\partial r}(\rho r v) = 0 \tag{1}$$

Momentum:

$$\frac{\partial}{\partial t}(\rho u) + \frac{\partial}{\partial x}(\rho u u) + \frac{1}{r}\frac{\partial}{\partial r}(\rho r v u) = -\frac{\partial p}{\partial x} + \mu\frac{\partial}{\partial x}\left(\frac{\partial u}{\partial x}\right) + \frac{\mu}{r}\frac{\partial}{\partial r}\left(r\frac{\partial u}{\partial r}\right) + \frac{\mu}{3}\frac{\partial}{\partial x}(\nabla\cdot\mathbf{V})$$

$$\frac{\partial}{\partial t}(\rho v) + \frac{\partial}{\partial x}(\rho u v) + \frac{1}{r}\frac{\partial}{\partial r}(\rho r v v) = -\frac{\partial p}{\partial r} + \mu\frac{\partial}{\partial x}\left(\frac{\partial v}{\partial x}\right) + \frac{\mu}{r}\frac{\partial}{\partial r}\left(r\frac{\partial v}{\partial r}\right) + \frac{\mu}{3}\frac{\partial}{\partial r}(\nabla\cdot\mathbf{V}) - \frac{\mu v}{r^2} \tag{2}$$

Energy:

$$\frac{\partial}{\partial t}(\rho T) + \frac{\partial}{\partial x}(\rho u T) + \frac{1}{r}\frac{\partial}{\partial r}(\rho r v T) = -\frac{1}{c_p}\left[\frac{\partial p}{\partial t} + \nabla\cdot(p\mathbf{V}) - p(\nabla\cdot\mathbf{V})\right] + \frac{k}{c_p}\frac{\partial}{\partial x}\left(\frac{\partial T}{\partial x}\right) + \frac{k}{c_p}\frac{1}{r}\frac{\partial}{\partial r}\left(r\frac{\partial T}{\partial r}\right) + \frac{\mu}{c_p}\left\{2\left[\left(\frac{\partial u}{\partial x}\right)^2 + \left(\frac{\partial v}{\partial r}\right)^2 + \left(\frac{v}{r}\right)^2\right] + \left(\frac{\partial v}{\partial x} + \frac{\partial u}{\partial r}\right)^2 - \frac{2}{3}(\nabla\cdot\mathbf{V})^2\right\} \tag{3}$$

where x and r are the axial and radial coordinates in cylindrical coordinate system, respectively; t is time; u and v are the velocity components in the axial an radial direction, respectively; T is temperature; p is pressure; k is thermal conductivity; c_p is the heat capacity at constant pressure; μ is dynamic viscosity; $\mathbf{V}$ is velocity vector; $\nabla\cdot\mathbf{V}$ represents the divergence of the velocity vector. Eqs. (1)–(3) can be transformed to the general curvilinear coordinate system by employing the chain rule. After some algebraic manipulations in order to put the equation in the conservative form, Eqs. (1)–(3) are rewritten as

Continuity:

$$\frac{\partial \rho}{\partial t} + \frac{1}{J}\frac{1}{r}\frac{\partial}{\partial \xi}(\rho r U) + \frac{1}{J}\frac{1}{r}\frac{\partial}{\partial \eta}(\rho r V) = 0 \tag{4}$$

Momentum:

$$\begin{aligned}
&\frac{\partial}{\partial t}(\rho u)+\frac{1}{J}\frac{1}{r}\frac{\partial}{\partial \xi}(\rho r U u)+\frac{1}{J}\frac{1}{r}\frac{\partial}{\partial \eta}(\rho r V u)\\
&\quad=-\frac{1}{J}\frac{\partial}{\partial x}\left(\frac{\partial p}{\partial \xi}r_\eta-\frac{\partial p}{\partial \eta}r_\xi\right)+\frac{1}{J}\frac{\mu}{3}\left[r_\eta\frac{\partial}{\partial \xi}(\nabla\cdot\mathbf{V})\right.\\
&\qquad\left.-r_\xi\frac{\partial}{\partial \eta}(\nabla\cdot\mathbf{V})\right]+\frac{1}{J}\frac{1}{r}\frac{\partial}{\partial \xi}\left(r\alpha\frac{\mu}{J}\frac{\partial u}{\partial \xi}-r\beta\frac{\Gamma_\phi}{J}\frac{\partial u}{\partial \eta}\right)\\
&\qquad+\frac{1}{J}\frac{\mu}{r}\frac{\partial}{\partial \eta}\left(r\gamma\frac{\Gamma_\phi}{J}\frac{\partial u}{\partial \eta}-r\beta\frac{\Gamma_\phi}{J}\frac{\partial u}{\partial \xi}\right)\frac{\partial}{\partial t}(\rho v)\\
&\qquad+\frac{1}{J}\frac{1}{r}\frac{\partial}{\partial \xi}(\rho r U v)+\frac{1}{J}\frac{1}{r}\frac{\partial}{\partial \eta}(\rho r V v)\\
&\quad=-\frac{1}{J}\frac{\partial}{\partial x}\left(\frac{\partial p}{\partial \xi}r_\eta-\frac{\partial p}{\partial \eta}r_\xi\right)\\
&\qquad+\frac{1}{J}\frac{\mu}{3}\left[r_\eta\frac{\partial}{\partial \xi}(\nabla\cdot\mathbf{V})-r_\xi\frac{\partial}{\partial \eta}(\nabla\cdot\mathbf{V})\right]\\
&\qquad+\frac{1}{J}\frac{1}{r}\frac{\partial}{\partial \xi}\left(r\alpha\frac{\mu}{J}\frac{\partial v}{\partial \xi}-r\beta\frac{\Gamma_\phi}{J}\frac{\partial v}{\partial \eta}\right)\\
&\qquad+\frac{1}{J}\frac{\mu}{r}\frac{\partial}{\partial \eta}\left(r\gamma\frac{\Gamma_\phi}{J}\frac{\partial v}{\partial \eta}-r\beta\frac{\Gamma_\phi}{J}\frac{\partial v}{\partial \xi}\right)
\end{aligned}\tag{5}$$

Energy:

$$\begin{aligned}
&\frac{\partial}{\partial t}(\rho T)+\frac{1}{J}\frac{1}{r}\frac{\partial}{\partial \xi}(\rho r U T)+\frac{1}{J}\frac{1}{r}\frac{\partial}{\partial \eta}(\rho r V T)\\
&\quad=-\frac{1}{c_p}\left[\frac{\partial p}{\partial t}+\nabla\cdot(p\mathbf{V})-p(\nabla\cdot\mathbf{V})\right]\\
&\qquad+\frac{\mu}{c_p}\left\{\frac{2}{J}\left[\left(r_\eta\frac{\partial u}{\partial \xi}-r_\xi\frac{\partial u}{\partial \eta}\right)^2+\left(x_\xi\frac{\partial v}{\partial \eta}-x_\eta\frac{\partial v}{\partial \xi}\right)^2\right]\right.\\
&\qquad+2J\left(\frac{v}{r}\right)^2+\frac{1}{J}\left[\frac{\partial}{\xi}(v r_\eta-u x_\eta)+\frac{\partial}{\partial \eta}(u x_\xi-v r_\xi)\right]^2\\
&\qquad\left.-\frac{2J}{3}(\nabla\cdot\mathbf{V})^2\right\}+\frac{1}{J}\frac{1}{r}\frac{\partial}{\partial \xi}\left(r\alpha\frac{1}{J}\frac{k}{c_p}\frac{\partial u}{\partial \xi}-r\beta\frac{1}{J}\frac{k}{c_p}\frac{\partial u}{\partial \eta}\right)\\
&\qquad+\frac{1}{J}\frac{\mu}{r}\frac{\partial}{\partial \eta}\left(r\gamma\frac{1}{J}\frac{k}{c_p}\frac{\partial u}{\partial \eta}-r\beta\frac{1}{J}\frac{k}{c_p}\frac{\partial u}{\partial \xi}\right)
\end{aligned}\tag{6}$$

where

$$\begin{aligned}
&U=u r_\eta-v x_\eta,\quad V=v x_\xi-u r_\xi\\
&\alpha=x_\eta^2+r_\eta^2,\quad \beta=x_\xi x_\eta+r_\xi r_\eta\\
&\gamma=x_\xi^2+r_\xi^2,\quad J=x_\xi r_\eta-x_\eta r_\xi
\end{aligned}\tag{7}$$

In Eqs. (4)–(7), U and V represent the contravariant velocity components, respectively; ξ and η are the curvilinear coordinates, respectively; J is the Jacobian determinant.

In this study, the heat conduction in the solid region and the flow in the gas region are solved separately and then coupled at the solid–gas interface. The boundary conditions for the governing equations have been shown in Fig. 2 and are described as follows. For the solid region, thermal radiation cooling is considered at the heated surface due to the high surface temperature. At the outer surface of the cylindrical solid, the thermally adiabatic condition is assumed. The boundary condition on the surface at the rear side is treated as natural air convection. For the gas region, the Mach number, temperature and flow angle (axial flow in this study) are prescribed at the inlet (in this study, the gas addition at the inlet mimics the gas release at the pyrolysis front). At the outlet (i.e., the heated surface), the static pressure is given, and the temperature at the outlet is evaluated by extrapolation from the near-interior node. The pyrolysis product is regarded as non-absorbing gas. For most of the simulation cases in this study, zero velocity boundary conditions are exerted on the gas–solid interface (i.e., $u=0$, $v=0$), which corresponds to the case in which no gas addition occurs along the channel wall. To account for the gas addition along the channel wall, non-zero boundary conditions shall be specified at the gas–solid interface (i.e., $u=0$, $v\neq 0$, where the gas addition velocity v is negative since it is in $-r$ direction).

3. Numerical algorithm

The governing Navier–Stokes equations are solved with the finite volume method (FVM) based on the SIMPLE algorithm (Patankar, 1980). The extension of the SIMPLE method by including the compressibility effect can be found in Karki and Patankar (1989), Demirdzic et al. (1993), Marchi and Maliska (1994), Rincon and Elder (1997), Date (1998). The contravariant components of the velocity are used as the dependent variables in the momentum equations. The collocated grid arrangement is adopted where all variables are stored at the control volume geometrical center. In this study, the body-fitted mesh is generated using the multisurface technique (Eiseman, 1985). The momentum interpolation technique (Rhie and Chow, 1983) is used to ensure the pressure–velocity coupling.

As previously stated, the heat conduction in the solid region and the flow in the gas region are solved separately and then coupled at the solid–gas interface. Therefore, the overall solution process is an iterative one. The numerical solution procedure at each time step is as follows:

(1) At the first time step, make an initial guess for the convection heat transfer coefficients at the solid–fluid interface. After the first time step, use the heat transfer coefficient calculated at the previous time step as the initial guess.
(2) Perform the heat conduction simulation in the solid region.
(3) After step (2), the solid temperatures at the solid–gas interface are known. This serves as the temperature boundary condition for the gas region. Then, the compressible gas flow simulation in the gas region is performed. After doing this, the convection heat transfer coefficients at the solid–fluid interface can be updated according to the temperature distribution in the gas region.
(4) Go back to step (2) and perform the heat conduction simulation in the solid region again with the most recently available convection coefficients, obtained from step (3), as the boundary condition.

Repeat the foregoing solution process until the changes of the temperature in the solid region are smaller than a prescribed minor tolerance (e.g., 10^{-4}). Because the Reynolds number is low for the microchannel gas flow, an underrelax technique is adopted to ensure a stable numerical algorithm. The time step is variable to capture the drastic temperature transients at the early stage of laser heating.

The FORTRAN computer codes are developed based on the above-mentioned numerical method and procedure. In the following, the credibility of the computer code for the 2D axisymmetric compressible gas flow is verified against two classical test problems.

The first test problem chosen is to test the effectiveness of the computer code in predicting subsonic flows. This flow is considered for the 10% bump channel with implied exit Mach number 0.5. In this case, stagnation pressure and temperature are specified at the inlet. At the exit, all the variables are extrapolated except for the static pressure which is prescribed. The geometry and the grid generation are shown in Fig. 3 (63×22 mesh). The Mach number distribution is shown in Fig. 4. The corresponding result by Date (1998) is also given. It can be seen that these two calculating results agree with each other very well.

The second test problem is for the supersonic flow in a 4% bump channel with an inlet Mach number 1.4. Since inlet Mach number is known, all variables at the inlet could be specified exactly. At the exit, all variables were linearly extrapolated. An 80×20 mesh is used for this case. Fig. 5 shows the comparison between the Mach number contours obtained by the present study and those by Date (1998). It is seen from Fig. 5 that, the shock wave effect due to supersonic flow is well captured using the present computer code. Once again, there is a good agreement between the present study and previous work (Date, 1998).

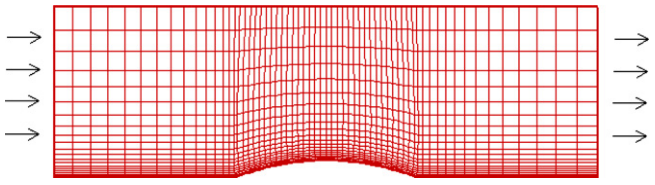

Fig. 3. Mesh for the compressible gas flow in a 10% bump channel.

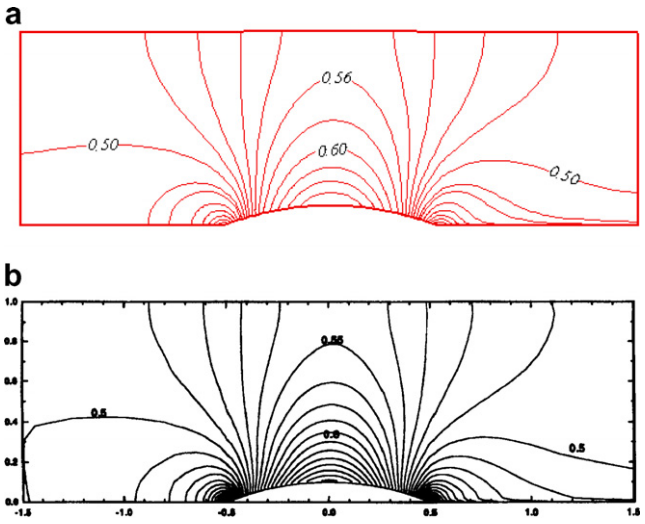

Fig. 4. Mach number distribution for subsonic flow (10% bump channel): (a) present study and (b) Date (1998).

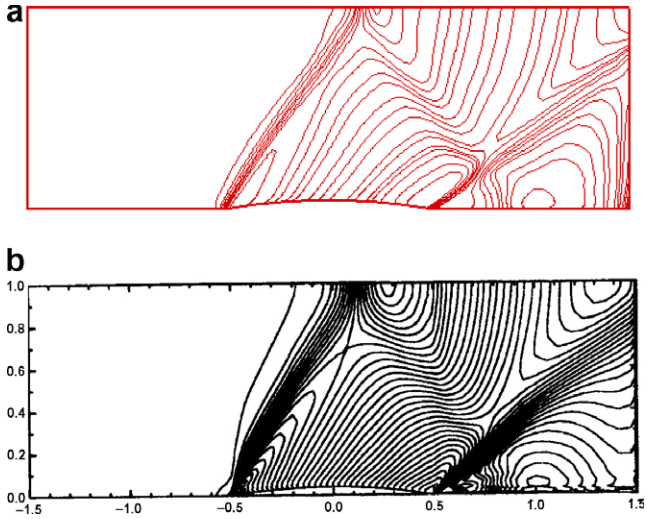

Fig. 5. Mach number distribution for supersonic flow (4% bump channel): (a) present study and (b) Date (1998).

4. Results and discussion

Once the computer code is validated, the numerical analysis for a solid medium with 200 μm thickness in x direction (as shown in Fig. 2) is performed. The material is initially at a uniform temperature, $T_i = 400$ K. For time $t > 0$, a constant heat flux of $q'' = 5$ MW/m^2 is impinged on the surface. After a grid convergence study, a 32×13 mesh is employed in the 2D compressible gas flow. The same mesh is used in the heat conduction simulation of the solid medium. The numerical solution is started from time $t = 0$ with a varying time step Δt (a small time step is used at early stage since the temperature rises drastically at this stage). The thermophysical properties of the solid medium used in the simulation are: $\rho_s = 1149.7$ kg/m^3, $c_{ps} = 1593.9$ J/(kg K), $k_s = 0.173$ W/(m K). The thermal properties of the gaseous byproducts are: $M = 28.97 \times 10^{-3}$ kg/mol, $c_{pg} = 1005$ J/(kg K), $Pr = 0.7$, $\mu = 1.81 \times 10^{-6}$ kg/(m s), $\gamma = 1.4$. By default, the Mach number and temperature at the gas flow inlet are 0.25 and 350 K, respectively. Other data are as follows: $T_\infty = 300$ K, $\varepsilon_{surf} = 0.92$, $h = 5$ W/(m^2 K).

The gas flow channel has the shape of a tapered cone. The inlet and outlet radii of the gas flow channel are 20 μm and 22 μm respectively, unless otherwise mentioned. There is no special rule for the choice of gas flow channel size. However, as mentioned earlier, to make the Knudsen number fall in the range in which the traditional Navier–Stokes equation remains valid, the radius of the gas flow channel must be greater than 15 μm (Schaff and Chambre, 1961). The outer radius of the solid material is assumed to be 40 μm.

Firstly, the necessity of accounting for the gas compressibility is examined when high-intensity heating is applied. Fig. 6 shows a comparison of the surface temperature–time curves obtained by the compressible (Mach number is 0.25) and incompressible models. It can be seen that, when the heat flux q'' is not very high, say less than 0.5 MW/m^2, there is insignificant difference between the results obtained by the compressible and incompressible model. However, as the heat flux q'' increases, for example, $q'' = 5$ MW/m^2, the difference becomes remarkable (e.g., the curves 2 and 4 in Fig. 6). This suggests that the compressibility of the gas flow be taken into account for severe thermal loading. All the subsequent calculations will be based on the compressible model.

Fig. 7 shows the predicted temperatures as a function of time at three different locations. As expected, the temperature rise at the point *a* (at the heated surface) is much larger than those at the quarter depth point *b* and the half depth point *c*. It is also seen that, for the case of high heat flux studied here, the temperature of the target increases drastically at early stage and reach a stable value very quickly.

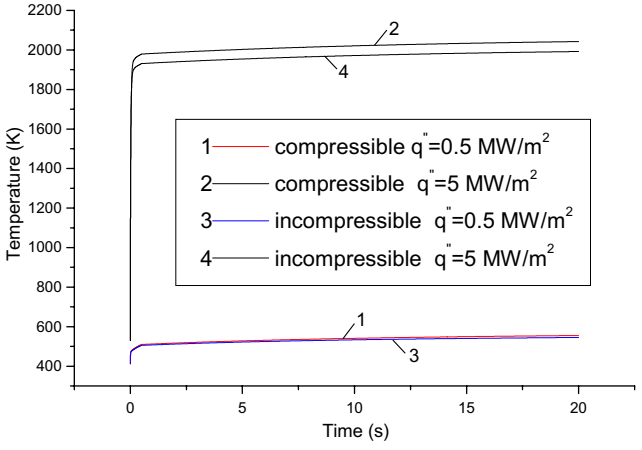

Fig. 6. Comparison of the results obtained by the compressible and the incompressible models. No gas addition is considered along the channel wall.

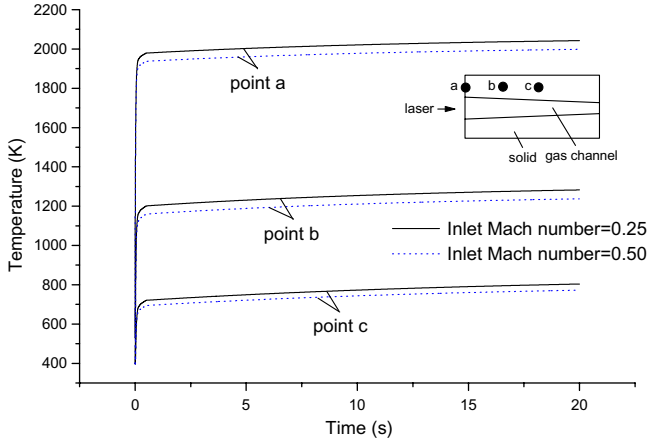

Fig. 7. Predicted temperatures as a function of time at three different locations. No gas addition is considered along the channel wall.

The sharp rise of the temperature can be well captured by the present numerical algorithm. Fig. 7 also presents a comparison between the case of inlet Mach number 0.25 and the case of inlet Mach number 0.50. As can be seen, the magnitude of the temperature rise for the case of higher inlet Mach number is smaller than that for the case of lower inlet Mach number. This is because that the higher inlet Mach number means a higher gas velocity at the pyrolysis front and, in turn, results in a stronger convective cooling effect along the solid–gas interface.

Fig. 8 gives the longitudinal Nusselt number Nu and centerline gas velocity distribution for different inlet Mach number at time $t = 10$ s. The Nusselt number Nu is defined as $Nu = h_{sg}D/k_g$, where h_{sg} is the convection heat transfer coefficient at the solid–gas interface, D is the diameter of the gas flow channel and k_g is the gas thermal conductivity. In Fig. 8, L_c is a characteristic length (in this study, L_c is chosen as the entrance radius of the gas flow channel). Nusselt number is a dimensionless group number, which is used to measure the importance of the convection heat exchange relative to the conduction heat exchange. It is observed from Fig. 8 that the higher the inlet Mach number, the larger the gas velocity (Fig. 8b) and the stronger

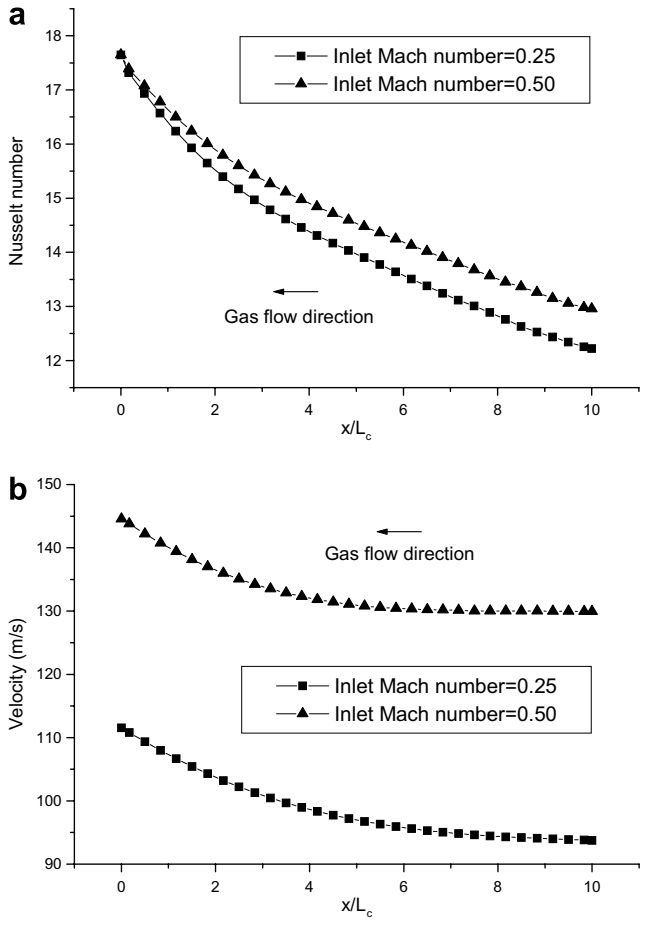

Fig. 8. The longitudinal Nusselt number and centerline gas velocity distributions for different inlet Mach number ($t = 10$ s). No gas addition is considered along the channel wall. (a) Nusselt number and (b) velocity.

the convection heat transfer effect. This is in good agreement with the temperature histories shown in Fig. 7. The inlet Mach number at the pyrolysis front is believed to be closely related to the thermal input. When the heat flux is high, the chemical reaction will take place very violently, and this will result in a large gas addition velocity at the pyrolysis front.

Fig. 9 presents the centerline normalized pressure distribution for different inlet Mach numbers. It is seen from this figure that the pressure decreases gradually from the pyrolysis front to the material surface. As expected, the gas flow for a higher Mach number needs to be driven by a larger pressure difference between inlet and outlet. However, even if the inlet Mach number is elevated from 0.25 to 0.5, there is no remarkable increase in the pressure difference between the pyrolysis front and target surface.

To further explore the reason for the small pressure difference, we have taken into account the effect of the gas addition along the channel wall. This means that the chemical reaction products enter the gas flow channel not only from the pyrolysis front but also from everywhere along the channel wall. This effect is implemented by introducing a non-zero v velocity boundary condition at the wall of the gas flow channel. The gas addition velocities in this study are estimated by combining the energy conservation equation at the solid–fluid interface and the following rate equation for the pyrolysis decomposition reaction

$$\frac{d\alpha}{dt} = A(1-\alpha)^M e^{B/T} \tag{8}$$

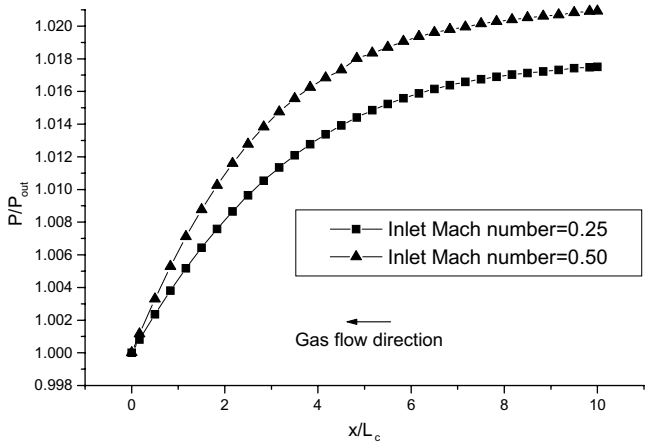

Fig. 9. Centerline normalized pressure distribution for different inlet Mach numbers ($t = 10$ s). No gas addition is considered along the channel wall.

where α is the fraction of decomposed material, t is time, A is called frequency factor, M is the order of the decomposition reaction, B is a constant determined by the activation energy and the universal gas constant. Calculations have been performed for the case where the inlet Mach number is 0.25 and the gas addition velocity is -1 m/s. The Mach number distribution in the flow channel for this case is shown in Fig. 10. It can be seen from this figure that, even though the flow cross-section area becomes larger and larger from the inlet to outlet, the gas velocity increases due to the gas mass addition from along the channel wall. The centerline normalized pressure distributions for different gas addition velocities are shown in Fig. 11. It is found that

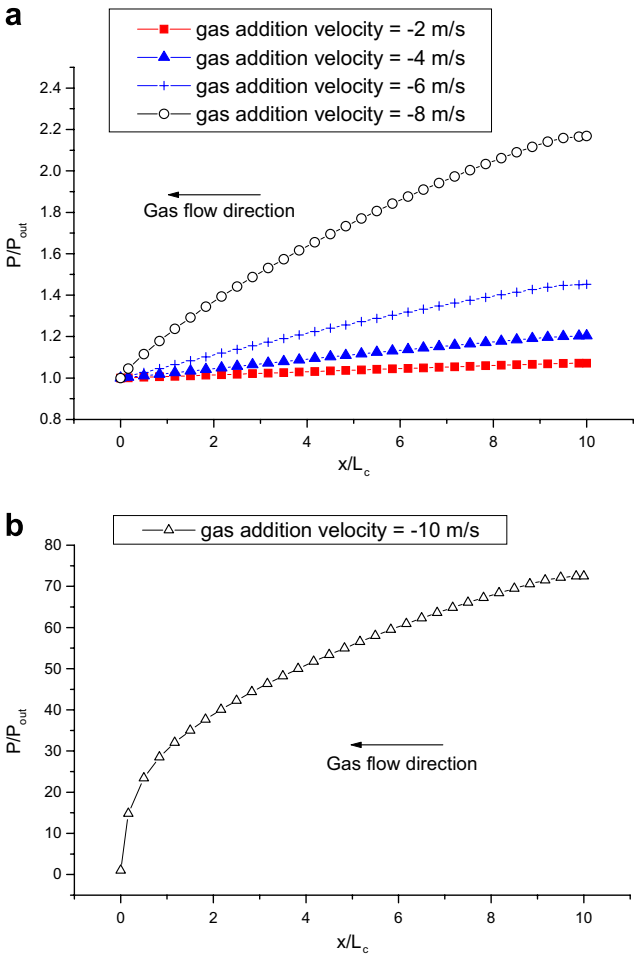

Fig. 11. Centerline normalized pressure distribution for the case of Mach number 0.25 ($t = 10$ s). Gas addition is considered along the channel wall.

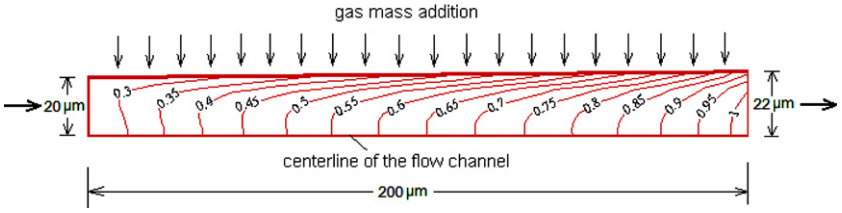

Fig. 10. Iso-Mach number distribution in the gas flow channel. Gas addition is considered along the channel wall.

the pressure difference between the inlet and outlet increases as the gas addition velocity from the flow channel wall rises. The increase is dramatic for higher gas addition velocities. When the gas addition velocity is increased to -10 m/s, the pressure at the pyrolysis zone is about 70 times higher than the pressure at the target surface, as shown in Fig. 11b. By comparing the results with those in Fig. 9, we may conclude that the pressure difference between the pyrolysis front and heated surface is essentially due to the gas mass addition along the channel wall. A fast gas addition is associated with a violent decomposition reaction, which is caused by a high heat flux applied. If combined with the structural analysis model, the resulting pressure information can also be used to predict the stress in the material and evaluate the failure characteristic of the irradiated material.

5. Conclusions

The compressible flow in a microchannel coupled with the heat conduction in the surrounding solid medium is investigated. The numerical model for the compressible flow is established in a non-orthogonal curvilinear coordinate system to accommodate the case of varying flow cross-section. The numerical code is validated against two test problems and good agreement is obtained. Numerical simulations are performed on the coupled flow and heat transfer behavior through a microchannel surrounded by solid media. The effect of the inlet Mach number on the Nusselt number is examined. The pressure distribution along the channel axial direction are obtained, which is helpful to the thermomechanical analysis of the composite material exposed to intensive laser heating. By imposing a non-zero v velocity boundary condition at the gas–solid interface, the influence of the gas addition along the channel wall on the pressure difference from the pyrolysis front to heated surface is discussed. It is shown that the pressure difference from the pyrolysis front to the target surface is caused essentially by the gas addition along the channel wall. If combined with the structural analysis model, the resulting pressure information can also be used to predict the stress in the material.

References

Beskok, A., Karniadakis, G.M., 1999. A model for flows in channels pipes and ducts at micro and nano scales. Microscale Thermophysical Engineering 3, 43–77.

Brannon, J.H., Lankard, J.R., Baise, A.I., Burns, F., Kaufman, J., 1985. Excimer laser etching of polyimide. Journal of Applied Physics 58 (5), 2036–2043.

Chen, C.-S., 2004. Numerical method for predicting three-dimensional steady compressible flow in long microchannels. Journal of Micromechanics and Microengineering 14, 1091–1100.

Chen, J.K., Perea, A., Allahdadi, F.A., 1995. A study of laser/composite material interactions. Composite Science and Technology 54, 35–44.

Date, A.W., 1998. Solution of Navier–Stokes equations on nonstaggered grid at all speeds. Numerical Heat Transfer Part B 33, 451–467.

Demirdzic, I., Lilek, Z., Peric, M., 1993. A collocated finite volume method for predicting flows at all speeds. International Journal for Numerical Methods in Fluids 16, 1029–1050.

Eiseman, P.R., 1985. Grid generation for fluid mechanics computations. Annual Review of Fluid Mechanics 17, 487–522.

Harley, J.C., Huang, Y., Bau, H.H., Zemel, J.N., 1995. Gas flow in microchannels. Journal of Fluid Mechanics 284, 257–274.

Karki, K.C., Patankar, S.V., 1989. Pressure based calculation procedure for viscous flows at all speeds in arbitrary configurations. AIAA Journal 27 (9), 1167–1174.

Kays, W.M., Crawford, M.E., 1980. Convective Heat and Mass Transfer. McGraw-Hill, New York.

Lane, R.J., Wynne, J.J., Geronemus, R.G., 1986. Ultraviolet laser ablation of skin: healing studies and a thermal model. Lasers in Surgery and Medicine 6, 504–513.

Lecartentier, G.L., Motamedi, M., McMath, L.P., Rastegar, S., Welch, A.J., 1993. Continuous wave laser ablation of tissue: analysis of thermal and mechanical events. IEEE Transactions on Biomedical Engineering 40 (2), 188–199.

Marchi, C.H., Maliska, C.R., 1994. A nonorthogonal finite-volume method for the solution of all speed flows using the co-located variables. Numerical Heat Transfer Part B 26, 293–311.

Patankar, S.V., 1980. Numerical Heat Transfer and Fluid Flow. Hemisphere, New York.

Rhie, C.M., Chow, W.L., 1983. Numerical study of the turbulent flow past an airfoil with trailing edge separation. AIAA Journal 21 (11), 1525–1532.

Rincon, J., Elder, R., 1997. A high-resolution pressure-based method for compressible flows. Computers and Fluids 26 (3), 217–231.

Schaff, S.A., Chambre, P.L., 1961. Flow of Rarefied Gases. Princeton University Press, Princeton, NJ.

Sobehart, J.R., 1993. Polyimide ablation using intense laser beams. Journal of Applied Physics 74 (4), 2830–2833.

Toh, K.C., Chen, X.Y., Chai, J.C., 2002. Numerical computation of fluid flow and heat transfer in microchannels. International Journal of Heat and Mass Transfer 45, 5133–5141.